

# Broad-band coupling of THz radiation to an $\text{YBa}_2\text{Cu}_3\text{O}_{7-\delta}$ hot-electron bolometer mixer

Yu P Gousev, A D Semenov, R S Nebosis, E V Pechen<sup>†</sup>,  
A V Varlashkin<sup>†</sup> and K F Renk

Institut für Angewandte Physik, Universität Regensburg, 93040 Regensburg,  
Germany

Received 22 May 1996

**Abstract.** We report on broad-band coupling of THz radiation to an  $\text{YBa}_2\text{Cu}_3\text{O}_{7-\delta}$  superconducting hot-electron bolometer. The bolometer—a micro-bridge of an  $\text{YBa}_2\text{Cu}_3\text{O}_{7-\delta}$  film with a  $\text{PrBa}_2\text{Cu}_3\text{O}_{7-\delta}$  protection layer—was built in a hybrid quasioptical antenna system consisting of a planar self-complementary spiral antenna on a dielectric substrate and an extended hyperhemispherical lens. The planar antenna was integrated into a coplanar transmission line for broad-band intermediate-frequency matching. Measurements performed in the direct detection regime between 2.5 THz and 4.2 THz delivered a system coupling efficiency for the radiation in the fundamental Gaussian mode of about 0.1 and a beam width of the radiation pattern of less than one degree. The pattern was consistent with the far-field radiation pattern that we calculated with a ray-tracing technique. At an intermediate frequency of 1.5 GHz we measured an output noise temperature of  $\approx 160$  K for the bolometer driven in the resistive state by both dc and THz current and estimated, for the heterodyne regime, a system noise temperature of  $\approx 3 \times 10^5$  K. We studied the effect of a protection layer on the rate of phonon escape from the micro-bridge and, thus, on the output frequency bandwidth of the device. We discuss possibilities of a significant improvement of the device performance.

## 1. Introduction

The THz frequency range is becoming increasingly important for radio astronomy, remote sensing of the upper atmosphere, plasma diagnostics, and other applications. The progress in these fields is in direct connection with the development of low-noise heterodyne receivers that are expected [1] to provide a better performance than Fourier transform instruments with direct detectors. The only practical heterodyne receiver which has been used up to now at frequencies above 1 THz is an open-structure corner reflector with a Schottky barrier diode as a mixing element [2, 3]. The lowest noise temperature of a Schottky diode receiver obtained so far at a frequency of 2.5 THz was around 12 000 K, mainly limited by noise in the diode (noise temperature  $\approx 8000$  K) [4]. At THz frequencies the video-responsivity of Schottky diodes drops approximately proportionally to the frequency [5], leading to a quadratic increase of the receiver noise temperature.

A few years ago the hot-electron bolometer (HEB) was proposed as a novel type of mixer having no spectral limitation in the far-infrared range [6, 7]. The mixer

employed an electron heating effect in either low- [8, 9] or high-temperature [10] superconducting thin films. The ultimate noise temperature of a HEB mixer ideally coupled with radiation was estimated to be between 50 K and 500 K depending on the superconducting material (Nb, NbN or  $\text{YBa}_2\text{Cu}_3\text{O}_{7-\delta}$ ) [6, 11]. The input (radio-frequency) and output impedances of a mixer are almost real [6, 12] and can be adjusted to a desired value by the proper choice of the device geometry. A relatively good performance of HEB mixers was demonstrated at frequencies up to 600 GHz [13, 14] in a waveguide design. At higher frequencies a decrease of the radiation coupling efficiency significantly decreased the mixer sensitivity [15].

In principle, THz radiation can be coupled to a HEB mixer by use of different antennas, such as corner reflectors, corrugated horn antennas [16], a parabolic reflector combined with a planar antenna array [17], a tapered slotline antenna [18], and others; a review of antennas, most of which could be used in the THz range, is given in [19]. The corner reflector is, most likely, the best solution for Schottky diode receivers, but not for all detectors, because of relatively large side lobes of the radiation pattern, which do not lie in either *E*- or *H*-planes [20], a high cross-polarization level, and a strong limitation due to the finite diameter of the antenna whisker.

<sup>†</sup> Permanent address: Lebedev Physics Institute of RAS, 117924 Moscow, Russia.

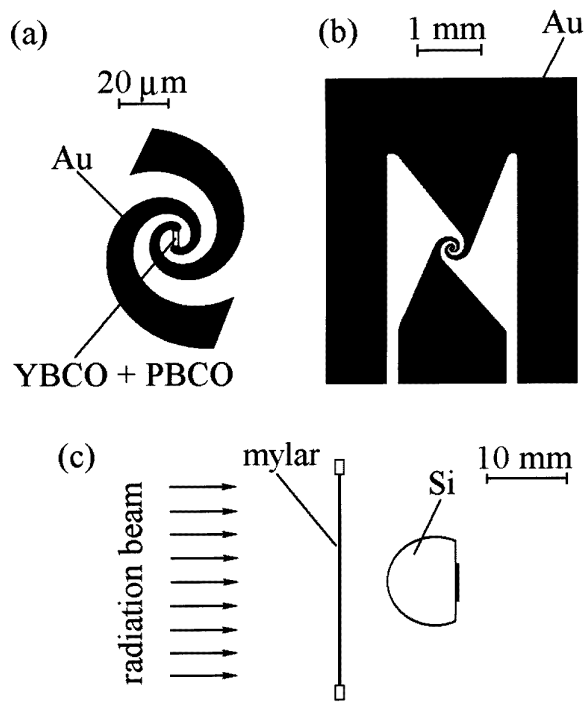


**Figure 1.** A superconducting micro-bridge connected to a gold spiral antenna (a), the antenna integrated into a coplanar line (b), and a quasi-optical system (c).

One of the most promising antenna designs for THz frequencies is an integrated system with a dielectric substrate, carrying a planar feed antenna with a sensitive element, clamped on the back of an immersion lens [21]; preliminary focusing of the radiation is normally required. The feed antenna may be of bow-tie, logarithmic spiral, log-periodic, double-dipole, or double-slot configuration; all of the antenna types have a rather low directivity in free space and, therefore, require an immersion lens. The majority of integrated receivers [21, 22] employed a hyperhemispherical immersion lens [23], with the feed antenna placed at the distance  $r/n$  behind the centre of the hemisphere ( $r$  is the radius of the hemisphere,  $n$  the refractive index of the lens) whereby aberrations were small.

A new design of an integrated receiver was proposed [24] for imaging array optics. In this approach an immersion lens has such an extension length that the feed antenna is placed between the hyperhemispherical position and the elliptical focus (the second focus of the elliptical lens may be synthesized by use a hemispherical lens with an appropriate extension length [24, 25]). In this case the immersion lens and the planar antenna work as a single hybrid antenna with a radiation pattern close to the diffraction limit determined by the cross section of the lens; no complicated optics is required to couple a single-mode radiation to the hybrid antenna. Hybrid antennas have been used successfully at frequencies up to  $\approx 600$  GHz [24, 25].

In this paper we report on efficient, broad-band coupling of THz radiation to an  $\text{YBa}_2\text{Cu}_3\text{O}_{7-\delta}$  (YBCO) superconducting HEB by means of a hybrid antenna. Using

a direct detection regime, we studied the radiation pattern of the antenna for frequencies between 2.5 THz and 4.2 THz. Analysing current–voltage characteristics of the HEB with and without irradiation, we obtained the efficiency of the radiation coupling and determined losses in the quasi-optical components. We have studied the influence of a protection layer covering the HEB on the output frequency bandwidth of the device. Finally, making use of the measured value of the mixer output noise, we estimated for our device the performance expected for operation in the heterodyne regime.

## 2. Experimental procedure

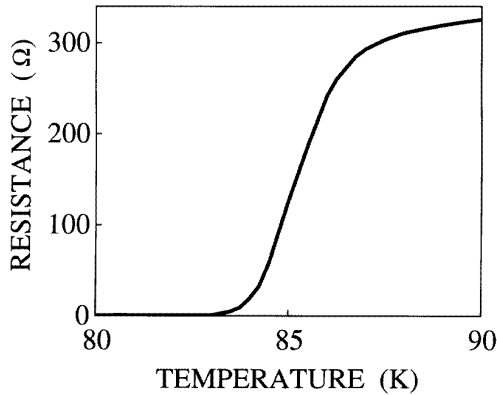
The HEB was an YBCO micro-bridge integrated into a gold planar self-complementary spiral feed antenna on a dielectric substrate (figure 1(a)). The inner and outer diameters of the antenna were  $\approx 10 \mu\text{m}$  and  $\approx 0.4$  mm, respectively, thus limiting the operation range to radiation frequencies between 0.8 THz and 6 THz. The antenna arms were connected to a broad-band coplanar transmission line (figure 1(b)). The substrate with the antenna was clamped with the rear side on an extended hyperhemispherical silicon lens (radius 6.3 mm). The distance between the centre of the lens and the feed antenna was about 2.5 mm; the extension length was chosen following the concept of the hybrid antenna [24]. No anti-reflection coating of the silicon lens was used. The device was mounted on a cold finger of a variable-temperature cryostat with optical access through a Mylar window (figure 1(c)); a dc current was supplied via a bias tee.

For preparation of samples we first grew on a (100)-oriented MgO substrate (thickness 0.5 mm) an YBCO film (thickness 25 nm to 35 nm), then a  $\text{PrBa}_2\text{Cu}_3\text{O}_{7-\delta}$  (PBCO) protection layer (8 nm to 50 nm), and finally a gold film (200 nm to 230 nm). We used a pulsed-laser ablation technique with a synchronous velocity filtration of the laser-induced plasma to eliminate macro-particles and droplets [26]; the radiation of an excimer laser (wavelength 308 nm, pulse duration 15 ns, repetition rate 8–25 Hz) was focused on a disk-shaped rotating target while the pulse energy density was  $10\text{--}20 \text{ J cm}^{-2}$ . We deposited an Y–Ba–Cu–O target to a Pr–Ba–Cu–O target and then to an Au metal target *in situ* in a vacuum chamber. The YBCO film and the PBCO protection layer were grown in an oxygen atmosphere at a pressure of 0.15 mbar on a substrate heated to a temperature of  $670^\circ\text{C}$ . Then, we filled the chamber with oxygen up to a pressure of 0.8 bar, cooled the sample to room temperature, evacuated the chamber to a pressure of  $10^{-6}\text{--}10^{-5}$  mbar, and, finally, deposited the gold layer also by laser ablation. The thicknesses of the YBCO films, the PBCO protection layers, and the Au films for four samples are given in table 1.

The structuring of the samples was performed in two steps, each including photolithography and chemical etching. In the first step, we applied a positive photoresist mask to shape the coplanar waveguide, the feed antenna, and the micro-bridge with an area of several square

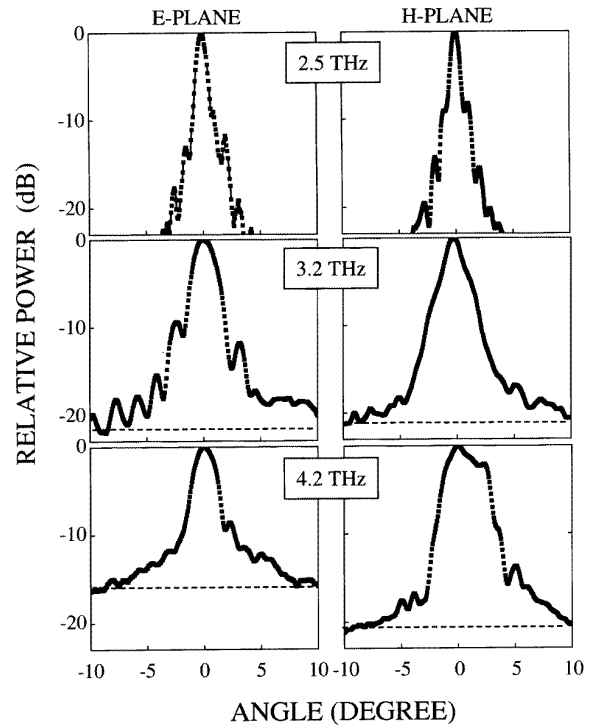
**Table 1.** Parameters of samples.

	No 1	No 2	No 3	No 4
Transition temperature (K)	85.5	87.7	89	88.5
Transition width (K)	2	3	2	2.5
Normal-state resistance ( $\Omega$ )	320	200	120	180
YBCO film thickness (nm)	34	26	50	28
PBCO film thickness (nm)	34	9	50	8
Gold film thickness (nm)	200	200	230	200
Micro-bridge size ( $\mu\text{m}^2$ )	$9 \times 3$	$4 \times 3$	$3.5 \times 3$	$4 \times 3$
Phonon escape time (ns)	2.4	1.3	3.4	—

**Figure 2.** Sample resistance.

microns. To remove the gold gently with minimal under-etching, we used an ethylene glycol solution containing  $\text{I}_2$  and  $\text{NaI}$ ; a 10% solution of  $\text{NaI}$  in water-free ethylene glycol was saturated with  $\text{I}_2$  (concentration  $\sim 40\%$ ). Due to the high viscosity of ethylene glycol only a thin layer of the reagent near the sample surface was involved in the reaction because of a decrease of the concentration of reactive ions; it significantly reduced the under-etching at the contour edges. For etching PBCO layers and YBCO films a solution of 2.5%  $\text{HNO}_3$  in ethylene glycol was used. At the second stage, applying another photoresist mask, we removed again with the  $\text{I}_2$ - $\text{NaI}$  solution the gold layer from the micro-bridge.

A typical temperature dependence of the micro-bridge resistance showed a linear decrease between room temperature and 90 K and a superconducting transition within few K (figure 2). While the use of water-containing  $\text{I}$ - $\text{NaI}$  and  $\text{I}$ - $\text{KI}$  solutions caused a noticeable degradation of the superconducting properties, etching of gold with concentrated ethylene glycol solution resulted only in a slight change of the superconducting transition of the micro-bridge with respect to the unstructured film. We observed, when using water-free solutions, a 2–3 K reduction of the transition temperature  $T_c$  (determined as the temperature corresponding to the midpoint of the transition) and an increase of the width of the superconducting transition by a factor of  $\approx 2$ . The transition temperature (table 1) was smaller for thinner YBCO films; we found no correlation between  $T_c$  and the thickness of the PBCO protection layer. The thickness of a protection layer as small as 10 nm

**Figure 3.** The radiation pattern of the hybrid antenna with the extended hyperhemispherical lens in two perpendicular planes at 2.5 THz, 3.2 THz, and 4.2 THz. Noise levels are shown by horizontal (dashed) lines.

provided a good stability of the superconducting properties of our samples over several months.

For studying the radiation properties of the hybrid antenna we operated the HEB as a direct detector for chopped cw laser radiation. Irradiation resulted in an increase of the sample resistance and, therefore, led to a voltage change across the micro-bridge connected to a dc current source. The change of voltage at the micro-bridge was measured using a lock-in technique. The ambient temperature was  $\approx 1.5$  K below  $T_c$  resulting in a sample dc resistance of  $\approx 100 \Omega$  at a bias current of few mA. The antenna was irradiated by an almost parallel beam (divergence  $1^\circ$ ) of a far-infrared gas laser (frequencies 2.5 THz, 3 THz, or 4.2 THz) operated in the regime of the fundamental Gaussian mode; the distance from the waist of the laser beam was  $\approx 1.7$  m. The power density of the radiation was measured in the plane of the cryostat

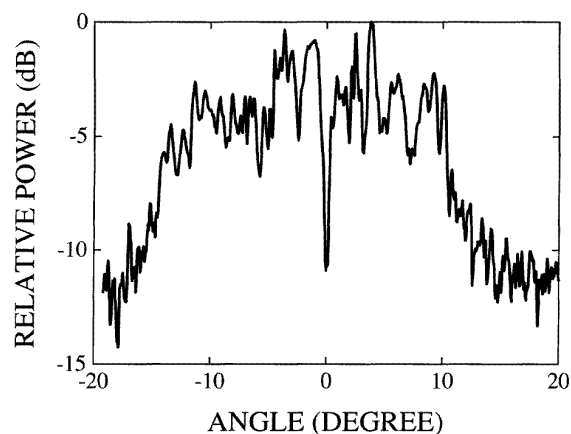


**Figure 4.** The radiation pattern of the antenna with the hyperhemispherical lens for 2.5 THz radiation.

window by a calibrated Golay cell detector. We measured the radiation pattern by rotating the antenna in the electric field plane of the incident radiation around the axis either coinciding with ( $H$ -plane) or perpendicular to ( $E$ -plane) the axis of the coplanar line and obtained the dependence of the power absorbed by the HEB on the angle of incidence; the voltage change across the HEB was proportional to the radiation power. To change the rotation axis we completely reinstalled the sample; that partially could account for the difference between  $E$ - and  $H$ -plane patterns for the same sample (see below). The output noise temperature of the device was measured with and without irradiation using a low-noise amplifier and a spectrum analyser.

### 3. Experimental results

#### 3.1. Radiation properties of the hybrid antenna

The radiation pattern of the hybrid antenna at a radiation frequency of 2.5 THz (figure 3, upper part) consisted of a narrow main lobe and a side-lobe structure. The main lobe had a full width (at a level of  $-3$  dB) of less than  $1^\circ$  in both planes; side lobes appeared below  $-8$  dB. Our result indicates that the radiation pattern of the hybrid antenna corresponded to an almost symmetric cone, according to the rotation symmetry of the radiation pattern of the spiral antenna.

At higher frequencies (figure 3) we obtained slightly broader and less symmetric radiation patterns. This was due to the misalignment of the spiral antenna with respect to the centre of the substrate lens, which is more critical at shorter wavelengths; the background was higher due to a smaller signal-to-noise ratio.

We measured the radiation pattern for our feed antenna also with a hyperhemispherical lens. The radiation pattern at 2.5 THz (figure 4) was broad (full width  $\approx 20^\circ$ ) and showed several maxima in the main lobe. At normal incidence we observed a dip (of about  $-10$  dB) with a width of  $\approx 1^\circ$ . Both the maxima and the dip may be due to interference effects in the lens.

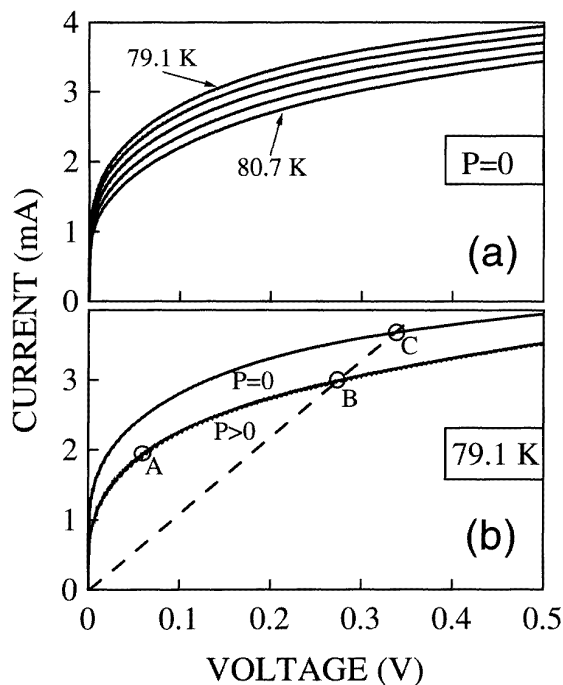


**Figure 5.** Current–voltage characteristics at different ambient temperatures (in steps of 0.4 K) without irradiation (a) and with radiation at a power density of  $1.1 \times 10^{-5} \text{ W cm}^{-2}$  (b).

#### 3.2. Current–voltage characteristics

Without irradiation, at an ambient temperature close to  $T_c$ , the current–voltage ( $V$ – $I$ ) characteristics of our samples were smooth; results for sample No 1 are shown in figure 5(a). The differential resistance was nearly zero at small voltages and increased to a constant value ( $670 \Omega$ ) at voltages between 0.3 and 0.5 V. Irradiation resulted in a decrease of the current while the differential resistance at high bias voltages remained approximately constant (figure 5(b)). Decreasing the ambient temperature with the radiation power applied we obtained a  $V$ – $I$  curve practically coinciding with one of those recorded at higher temperatures without irradiation. Thus, we suggest that the effect of the irradiation was essentially thermal and find a temperature shift of  $\approx 1.5$  K corresponding to a radiation power density of  $1.1 \times 10^{-5} \text{ W cm}^{-2}$  at the system input (in front of the Mylar window). Reducing of the power resulted in a corresponding proportional decrease of the temperature shift.

#### 3.3. Signal and noise characteristics

The dependence of the direct detection signal on the modulation (chopping) frequency was measured for the sample driven by both the dc current and cw radiation into the operation point (A, figure 5(b)). The dependence of the signal on the modulation frequency was weak (figure 6) and did not depend on the frequency of the THz radiation. The signal decreased between 10 Hz and  $10^4$  Hz approximately as  $f^{-\gamma}$  where  $f$  is the modulation frequency

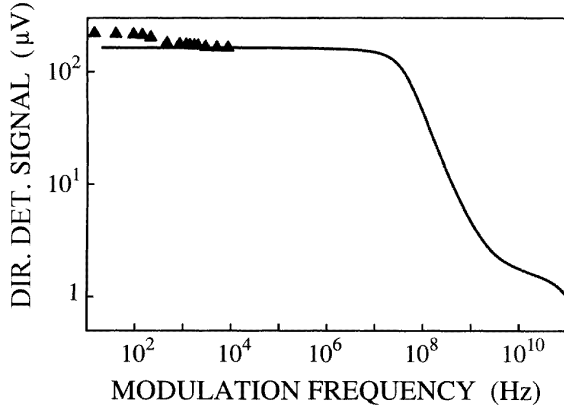


**Figure 6.** The direct detection response for different modulation frequencies. The solid line was calculated using equation (7).

and  $\gamma$  a parameter (between 0.02 and 0.1) that was sample dependent. We also determined the effective phonon escape time,  $\tau_{es}$ , for our samples measuring the real-time response to near-infrared radiation pulses (for experimental details see reference [27]). Using measured values of  $\tau_{es}$  we obtained a modulation frequency dependence of the response (the solid line in figure 6) which will be discussed later. Phonon escape times are presented in table 1. Though, in general, we found  $\tau_{es}$  increasing with the film thickness, it was not proportional either to the thickness of the YBCO or the PBCO layer or to the sum of these values.

The output noise temperature for sample No 1, irradiated at a power density of  $1.1 \times 10^{-5} \text{ W cm}^{-2}$  (operation point A, figure 5(b)), decreased gradually from  $\approx 280 \text{ K}$  at 100 MHz to  $\approx 160 \text{ K}$  at 1.4 GHz. At higher frequencies the noise temperature was nearly constant and was mainly determined by the Nyquist and thermal fluctuation noise; the contribution of each type of noise was determined in the same manner as described in [28]. We found similar values of output noise temperature when the sample was operated without THz irradiation and at almost zero bias current but at the same dc resistance. The result gives evidence that there was no contribution from the shot noise.

## 4. Discussion and numerical simulation

### 4.1. Radiation properties of the hybrid antenna

From the full width of the main lobe ( $\Theta_A \approx 1^\circ$ ) we estimate for the directivity  $D_0$  of the hybrid antenna, using the expression  $D_0 = 4\pi/\Theta_A^2$  [29],  $D_0 \approx 4 \times 10^4$  (46 dB) and a corresponding effective aperture  $A_{eff} = 4\lambda^2/D \approx 45 \text{ mm}^2$  where  $\lambda$  is the wavelength (119  $\mu\text{m}$ ) corresponding to the frequency 2.5 THz. A more accurate numerical calculation, including the part of the radiation in the side lobes, yields  $D = 10^4$  (40 dB). This value is very large and indicates that our antenna has an excellent performance; similar values are known for antenna arrays in the millimetre-wave range

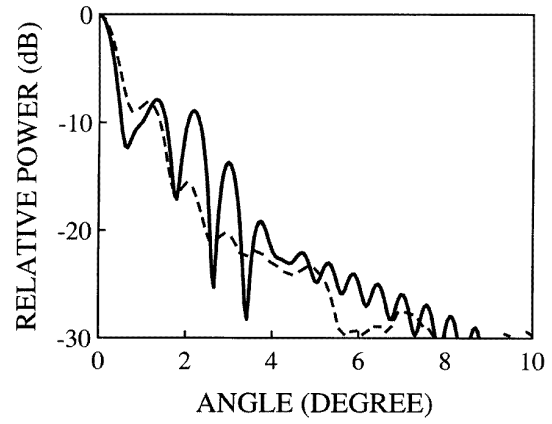


**Figure 7.** Calculated (solid line) and measured (dashed) radiation patterns at 2.5 THz for the hybrid antenna with the extended hyperhemispherical lens.

[30]. We calculated an overlap integral  $|\langle \Psi_A | \Psi_G \rangle|^2$  [19] for a Gaussian beam of the form

$$\Psi_G(\Theta) \sim \exp(-[\Theta/\Theta_0]^2) \exp(\pm i\pi[\Theta/\Theta_1]^2) \quad (1)$$

where  $\Theta$  is the angle of incidence of the radiation,  $\Theta_0$  and  $\Theta_1$  are characteristic angles for the amplitude and the phase, respectively, and  $\Psi_A(\Theta)$  describes the experimental radiation pattern of the hybrid antenna. Varying  $\Theta_0$  and  $\Theta_1$  we obtained for an overlap integral a value of 73% as the upper limit of the Gaussian coupling efficiency. Lower directivity, obtained at radiation frequencies above 2.5 THz, was most probably due to a misalignment of the feed antenna with respect to the centre of the silicon lens.

Using a ray-tracing technique, we have simulated a far-field radiation pattern of the hybrid antenna. First, we calculated the electric field distribution  $\mathbf{E}^{in}(\mathbf{r})$  on the inner surface of the immersion lens considering the feed antenna as an aperture of area  $A_0$  radiating in a homogeneous dielectric medium, and assuming that the phase and the amplitude of the electromagnetic field are constant in the aperture plane. The electric field produced by the feed antenna in a point defined by the radius vector  $\mathbf{r}$  is given by

$$\mathbf{E}^{in}(\mathbf{r}) = \int_{-\infty}^{+\infty} \mathbf{E}_{ap}(\mathbf{r}') G(|\mathbf{r}' - \mathbf{r}|) d\mathbf{r}' \quad (2)$$

where  $\mathbf{r}'$  is the radius vector of the radiating segment of the aperture,

$$G(|\mathbf{r}' - \mathbf{r}|) = e^{ik|\mathbf{r}' - \mathbf{r}|} / (4\pi|\mathbf{r}' - \mathbf{r}|) \quad (3)$$

is the Green's function for a homogeneous medium,  $\mathbf{k}$  is the wave vector of the radiation in the dielectric, and  $i = \sqrt{-1}$ . The initial electric field distribution,  $\mathbf{E}_{ap}(\mathbf{r}')$ , of the feed antenna was determined by summarizing over all radiating segments of the aperture. The number of segments was chosen so that  $d\mathbf{r}$  was small compared to the wavelength of the radiation in the lens. Using boundary conditions for the silicon-vacuum interface  $E_{\parallel}^{in} = E_{\parallel}^{out}$ ,  $E_{\perp}^{in} = \sqrt{\epsilon} E_{\perp}^{out}$  with  $E_{\parallel}$  and  $E_{\perp}$  being the tangential and the normal components of the electric field on the inner

(*in*) and the outer (*out*) surfaces of the silicon lens, and  $\varepsilon$  the dielectric constant of the lens material, we obtained the electric field distribution on the outer surface. Finally, using equation (2) for vacuum, we calculated the electrical field distribution in the plane at a distance 100 mm away from the lens and obtained the far-field radiation pattern of the hybrid antenna. The radiation pattern calculated for the 2.5 THz radiation frequency (with the best-fit value  $A_0 = 7.3 \times 10^{-5} \text{ cm}^2$ ) shows (figure 7) good agreement with the experiment.

We also calculated the far-field radiation pattern of the feed antenna without a lens and obtained for the free space a half-power full width of  $65^\circ$  in agreement with the experimental pattern [31] that has been measured for the complementary spiral antenna.

#### 4.2. Efficiency of the radiation coupling

We calculated the efficiency of the radiation coupling as the ratio of the radiation power,  $P_{ab}$ , absorbed in the micro-bridge and the power,  $P$ , of radiation incident on the hybrid antenna. We obtained  $P$  from the radiation power density in the centre of the beam,  $p_0$ , and the effective aperture  $A_{eff}$  of the hybrid antenna according to  $P = p_0 A_{eff}$ . We found  $P \approx 5 \text{ mW}$  for the lower  $V$ - $I$  curve of figure 5(b). Neglecting nonthermal effects of the current on the resistance of the micro-bridge we assumed that, for currents large compared to the critical current, the resistance was a function of the effective electron temperature only [32]. Since both the Joule power and radiation power are primarily absorbed by electrons, the heating of the micro-bridge by the current is of the same type as that by radiation. A change of the electron temperature,  $\Delta T_e$ , in a steady state, due to the current and the radiation, is then given by

$$\Delta T_e = T_e - T_0 = \Re_0 [P_{ab} + I^2 R(T_e)] \quad (4)$$

where  $T_0$  is the ambient temperature,  $I$  the current,  $R$  the dc resistance of the micro-bridge, and  $\Re_0$  the effective thermal resistance between the electron system and thermostat. Comparing two operation points (B and C, figure 5(b)) with the same dc resistance ( $\approx 100 \Omega$ ; the dashed line of figure 5(b)) and, thus, with the same electron temperature, we concluded that the decrease of the Joule power (0.5 mW at the operation point B) was compensated by the absorbed radiation power. With  $P_{ab} = 0.5 \text{ mW}$  we found a system coupling efficiency of  $\approx 0.1$ . Taking into account loss (0.1) at the Mylar window, reflection loss (0.3) at the front surface of the silicon lens, polarization loss (the spiral antenna is sensitive to circularly polarized radiation), and loss (0.3) due to impedance mismatch between the micro-bridge and the antenna (we assumed that the antenna has an impedance of  $377[2(1 + \varepsilon)]^{-0.5} \Omega$ ), we estimated for the antenna a coupling efficiency of 0.6, that was slightly lower than the calculated maximum Gaussian coupling efficiency (0.73). The difference may be attributed to nonperfect matching of the laser beam to the antenna (we measured the coupling efficiency in a slightly divergent beam), dielectric loss in the immersion lens, and conductor loss in the planar antenna. The system coupling efficiency can still

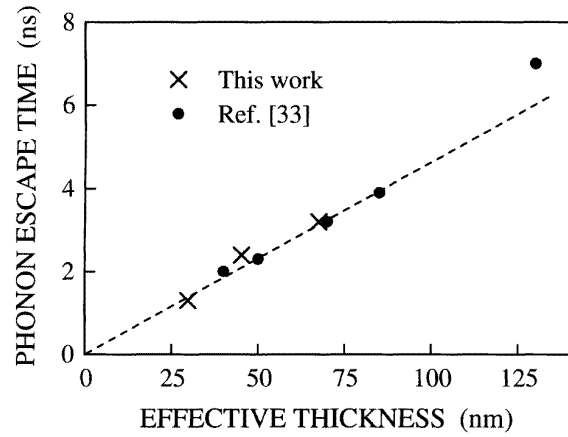


**Figure 8.** Phonon escape times. The dashed line is a guide for the eyes.

be increased using an anti-reflection coating for the lens and eliminating the impedance mismatch.

We also measured the coupling efficiency for our feed antenna combined with a hyperhemispherical lens. We used a preliminary focused convergent beam with an angle of convergence equal to the width of the main lobe of the radiation pattern ( $\approx 20^\circ$ , figure 4). We obtained a system coupling efficiency of  $\approx 0.03$  that was one third of that for the hybrid antenna with the extended hyperhemispherical lens. Recently, it has been reported [25] that at lower radiation frequencies the calculated Gaussian coupling efficiency was larger for the hyperhemispherical lens. Our results showed the opposite behaviour. This might be due to the breaking down of the Gaussian formalism for large angles of convergence [24].

#### 4.3. Signal characteristics in the direct detection regime

We now evaluate the time of phonon escape from a two-layer YBCO/PBCO system, with the thicknesses  $d_1$  (YBCO) and  $d_2$  (PBCO), to the substrate. We assume that (1) the lattice parameters of YBCO and PBCO are identical and there is no thermal boundary resistance between the YBCO and PBCO layers; (2) the thickness of the YBCO/PBCO system  $d_1 + d_2$  is smaller than  $l_{ph}/\beta$  ( $l_{ph} \geq 200 \text{ nm}$  [33] is the phonon mean free path in YBCO and PBCO,  $\beta < 1$  the average transparency coefficient for phonons incident from the YBCO film onto the substrate). Under these conditions the time of the phonon escape from the homogeneously heated YBCO/PBCO system is given by [33]

$$\tau_{es0} = 4d/(\beta u) \quad (5)$$

where  $u$  is the average group velocity for all phonon modes and  $d = d_1 + d_2$ . Since there are almost no free carriers in the PBCO layer, the radiation is mainly absorbed in the YBCO film. A nonequilibrium phonon can propagate with the same probability to the direction of the PBCO layer or to the direction of the substrate. Half of the phonons cross the YBCO/PBCO interface and escape to the substrate with a characteristic time  $\tau_{es1} \approx 4(d_1 + d_2)/(\beta u)$ . The other

**Table 2.** Physical parameters of YBCO and MgO.

	YBCO	MgO
Electron–phonon interaction time (ps)	2.0	—
Phonon specific heat (J K <sup>-1</sup> cm <sup>-3</sup> )	0.9	0.53
Electron specific heat (J K <sup>-1</sup> cm <sup>-3</sup> )	0.022	—
Thermal conductivity (W K <sup>-1</sup> cm <sup>-1</sup> )	—	3.4

half of the phonons escape to the substrate with a time  $\tau_{es2} \approx 4d_1/(\beta u)$ . An effective escape time  $\tau_{es}$  is then given by  $\tau_{es}^{-1} = 0.5(\tau_{es1}^{-1} + \tau_{es2}^{-1})$ . This value coincides with the escape time of phonons from a homogeneous YBCO film with the thickness

$$d_{eff} = d_1[1 + d_2/(2d_1 + d_2)]. \quad (6)$$

The escape time that we measured for our samples was almost proportional (figure 8) to the effective thickness calculated according to equation (6). Our result is consistent with data [33] (also shown in figure 8) for escape times measured for unprotected ( $d_2 = 0$ ) YBCO films on MgO substrates.

We now evaluate the frequency dependence of the responsivity. In our case, the equivalent resistance of the output circuit (the input resistance of the lock-in amplifier) was infinitely large compared to that of the HEB, thus allowing us to simplify the general expression for the responsivity [11] to

$$\begin{aligned} S(\omega) &= \alpha I \frac{dR}{dT_e} \Delta T_e / P \\ &= \alpha I \frac{dR}{dT_e} \Re(\omega) \frac{1}{1 - \Re(\omega) I^2 (dR/dT_e)} \end{aligned} \quad (7)$$

where  $\alpha$  is the effectiveness of the radiation coupling,  $\omega = 2\pi f$  the modulation frequency, and  $\Re(\omega)$  the frequency-dependent effective thermal resistance between electrons in the HEB and the bath;  $\Re_0 = \Re(0)$  was used in equation (4) for steady-state conditions. Recent studies [27, 34] have shown that the voltage response of an YBCO HEB can be adequately described in terms of the relaxation of the effective electron and phonon temperatures where the change of the phonon temperature in the substrate is included. Accordingly, the effective thermal resistance is then combined [35] from two terms corresponding to the heat transfer from electrons to the substrate ( $\Re_e$ ) and the heat diffusion in the substrate ( $\Re_s$ ):

$$\Re(\omega) = \Re_e(\omega) + \Re_s(\omega) \quad (8)$$

$$\Re_e(\omega) = \frac{\tau_{ep} + \tau_{es} c_e / c_p}{c_e v} \sqrt{\frac{1 + (\omega \tau_{ep} c_p / c_e)^2}{(1 + (\omega \tau_{ep})^2)(1 + (\omega \tau_{es})^2)}} \quad (9)$$

$$\Re_s(\omega) = \left\{ K_s \sqrt{2\pi B} \sqrt{\left(1 + \sqrt{\frac{C_s B \omega}{4\pi K_s}}\right)^2 + \frac{C_s B \omega}{4\pi K_s}} \right\}^{-1} \quad (10)$$

where  $c_e$  is electron and  $c_p$  the phonon specific heat,  $\tau_{ep}$  the electron–phonon interaction time,  $v$  the volume,  $B$  the

lateral area of the YBCO micro-bridge,  $C_s$  the specific heat and  $K_s$  the thermal conductivity of the substrate. The values for YBCO [27] and MgO [33] are listed in table 2.

We calculated the effective amplitude of the signal  $\Delta U \approx S(\omega) P_S / (2\sqrt{2})$  ( $P_S$  is the modulated part of the radiation power) for sample No 1 (figure 6, solid line) with  $\tau_{es} = 2.4$  ns,  $I \approx 2$  mA (operation point A, figure 5(b)),  $\alpha = 0.1$ ,  $P_S = 10^{-3} P$ , and  $dR/dT_e \approx 100 \Omega \text{ K}^{-1}$ . The temperature derivative of the sample resistance corresponding to the dc resistance at the operation point ( $\approx 30 \Omega$ ) was obtained from the  $R(T)$ -dependence (figure 2), measured at almost zero current without irradiation ( $dR/dT$  was then close to  $dR/dT_e$ ). For a modulation frequency of  $10^4$  Hz we found that the calculated signal was close to the experimental value while at zero frequency the experimental value was  $\approx 20\%$  larger, most probably due to a thermal resistance between the substrate and the cold finger of the cryostat.

#### 4.4. The performance of the HEB in the heterodyne regime

The conversion gain of a HEB mixer is determined [6] by the frequency-dependent voltage responsivity,  $S(\omega)$ , according to

$$\eta(\omega) = 2\alpha S(\omega)^2 P R_L^{-1} \quad (11)$$

where  $R_L$  is the equivalent resistance of a circuit connected to the mixer output and  $P$  the power of radiation delivered by a local oscillator (a laser in our case). In the heterodyne regime, when  $R_L$  is comparable with the impedance of the mixer, the responsivity is given by [12, 35]

$$\begin{aligned} S(\omega) &= \alpha I \frac{dR}{dT_e} \Re(\omega) \\ &\times \frac{1}{\Re(\omega) I^2 (dR/dT_e) (R/R_L - 1) + Z(\infty)/R_L + 1} \end{aligned} \quad (12)$$

where  $Z(\infty)$  is the impedance of the mixer at an infinitely large frequency. The single-side-band noise temperature of the receiver is

$$T_{SSB} = \eta^{-1} T_{out} \quad (13)$$

where  $T_{out}$  is the output noise temperature of the mixer. To estimate mixer performance we assumed  $R_L = 50 \Omega$  and  $Z(\infty) = R$  [11]. Using experimental parameters (operation point A, figure 5(b)) and the calculated value of the effective thermal resistance (equations (9), (10)) we found  $\eta \approx 5 \times 10^{-4}$  at a frequency of 1.5 GHz. With our experimental values of the output noise temperature we obtained a receiver noise temperature of  $2 \times 10^4$  K at zero intermediate frequency and  $3 \times 10^5$  K at 1.5 GHz.

We should note that the receiver noise temperature was calculated using our experimental values of the operation temperature and available power of the local oscillator while the estimated optimal power at 79.1 K was  $\approx 5$  times the power of the laser radiation in our experiment. Therefore, we believe that operating our HEB at a lower temperature ( $\approx 70$  K) and a higher local oscillator power should lead to a 30–100 times larger conversion gain in accordance with equation (11). In addition, the radiation

coupling loss may be reduced by using an anti-reflection coating for the lens and adjusting the mixer impedance to the impedance of the antenna. Since our planar antenna is frequency independent, and the output noise temperature of a HEB under optimal conditions is nearly constant over a wide range of operation temperatures [28], we suggest that a receiver noise temperature of less than  $10^4$  K and an intermediate-frequency band of more than 10 GHz may be reached at radiation frequencies up to  $\approx 6$  THz. The use of another immersion lens (absorption in Si becomes significant above 6 THz) and a smaller inner diameter of the feed antenna may extend the range of operation up to  $\approx 30$  THz.

## 5. Conclusion

We demonstrated that THz radiation can be effectively coupled to an YBCO superconducting hot-electron bolometer and we discussed possibilities for using the bolometer as a broad-band mixer for heterodyne detection of THz radiation. Because of the high directivity our quasioptical system allows a simple integration into a submillimetre telescope. We measured the aperture coupling efficiency and the output noise temperature of our device and estimated a receiver noise temperature of  $3 \times 10^5$  K at an intermediate frequency of 1.5 GHz. We suggest that the conversion gain can be 30–100 times larger if the mixer is operated at lower bath temperature and higher local oscillator power. The radiation coupling efficiency can be improved by using an anti-reflection coating for the lens, optimizing the extension length, using another planar antenna with a smaller polarization loss, and optimizing the impedance of the micro-bridge. We estimated for an optimized system a noise temperature of less than  $10^4$  K for radiation frequencies up to 6 THz. We also demonstrated that a thickness of the protection layer of less than 10 nm provided a long-term stability of the HEB and did not noticeably influence the performance of the device.

## Acknowledgments

The authors would like to thank M A Heusinger for measurements of the response to near-infrared laser pulses, as well as H S Barowski and A Arnold for making it possible to work with the far-infrared laser.

## References

- [1] Blundell R and Tong C Y E 1992 *Proc. IEEE* **80** 1702  
Miller S, Birk M, Schreier F and Hausamann D 1992 *Int. J. Infrared Millimeter Waves* **13** 1241
- [2] Röser H P 1991 *Infrared Phys.* **32** 385
- [3] Titz R, Birk M, Hausamann D, Nitsche R, Scheier F, Urban J, Küllman H and Röser H P 1995 *Infrared Phys.* **36** 883
- [4] Hübers H W, Crowe T W, Lundershauesen G, Peatman W G B and Röser H P 1993 *Proc. 4th Int. Symp. on Space Terahertz Technology (Los Angeles, CA)* (Los Angeles, CA: UCLA Press)
- [5] Hübers H M, Schwaab G W and Röser H P 1994 *J. Appl. Phys.* **75** 4243
- [6] Gershenzon E M, Gol'tsman G N, Gogidze I G, Gousev Yu P, Elant'ev A I, Karasik B S and Semenov A D 1990 *Sov. J. Supercond.* **3** 1582
- [7] Gershenzon E M, Gol'tsman G N, Elant'ev A I, Gousev Yu P and Semenov A D 1991 *IEEE Trans. Magn.* **27** 1317
- [8] Gershenzon E M, Gershenzon M E, Goltsman G N, Semenov A D and Sergeev A V 1984 *Sov. Phys.-JETP* **59** 442
- [9] Prober D E 1993 *Appl. Phys. Lett.* **62** 2119
- [10] Gershenzon E M, Gershenzon M E, Goltsman G N, Karasik B S, Semenov A D and Sergeev A V 1987 *JETP Lett.* **46** 285  
Aksaev E E, Gershenzon E M, Goltsman G N, Semenov A D and Sergeev A V 1989 *JETP Lett.* **50** 283  
Semenov A D, Goltsman G N, Gogidze I G, Sergeev A V, Gershenzon E M, Lang P T and Renk K F 1992 *Appl. Phys. Lett.* **60** 903
- [11] Karasik B S and Elantev A I 1995 *Proc. 6th Int. Symp. on Space Terahertz Technology (Pasadena, CA)* (Pasadena, CA: Californian Institute of Technology Press) p 229
- [12] Nebosis R S, Semenov A D, Gousev Yu P and Renk K F 1996 *Proc. 7th Int. Symp. on Space Terahertz Technology (Charlottesville, VA)* (Charlottesville, VA: University of Virginia Press)
- [13] Skalare A, McGrath W R, Bumble B, LeDuc H G, Burke P J, Verheijen A A and Prober D E 1995 *IEEE Trans. Appl. Supercond.* **5** 2236
- [14] Kawamura J, Blundell R, Tong C Y E, Gol'tsman G N, Gershenzon E M and Voronov B M 1996 *Proc. 7th Int. Symp. on Space Terahertz Technology (Charlottesville, VA)* (Charlottesville, VA: University of Virginia Press)
- [15] Gerecht E, Musante C F, Wang Z, Yngvesson K S, Muller E R, Waldman J, Gol'tsman G N, Voronov B M, Cherednichenko S I, Svechnikov S I, Yagoubov P A and Gershenzon E M 1996 *Proc. 7th Int. Symp. on Space Terahertz Technology (Charlottesville, VA)* (Charlottesville, VA: University of Virginia Press)
- [16] Clarricoats P J and Olver A D 1984 *Corrugated Horns for Microwave Antennas (IEE Electromagnetic Waves Series 18)* (London: IEE)
- [17] Filipovic D F, Ali-Ahmad W Y and Rebeiz G M 1992 *IEEE Trans. Microwave Theory Technol.* **40** 962
- [18] Gousev Yu P, Semenov A D, Nebosis R S, Renk K F, Gol'tsman G N, Karasik B S and Gershenzon E M 1996 *Int. J. Infrared Millimeter Waves* **17** 317
- [19] Rebeiz G M 1992 *Proc. IEEE* **80** 1748
- [20] Grossman E N 1989 *Infrared Phys.* **29** 875
- [21] Wengler M J, Woody D P, Miller R E and Phillips T G 1985 *Int. J. Infrared Millimeter Waves* **9** 101
- [22] Zmuidzinis J, Ugras N G, Miller D, Gaidis M C, LeDuc H G and Stern J A 1995 *IEEE Trans. Appl. Supercond.* **5** 3053
- [23] Rutledge D B and Muha M S 1982 *IEEE Trans. Antennas Propag.* **30** 535
- [24] Büttgenbach T H 1993 *IEEE Trans. Microwave Theory Technol.* **41** 1750
- [25] Filipovic D F, Gearhart S S and Rebeiz G M 1993 *IEEE Trans. Microwave Theory Technol.* **41** 1738
- [26] Pechen E V, Varlashkin A V, Krasnosvobodtsev A I, Brunner B and Renk K F 1995 *Appl. Phys. Lett.* **66** 2292
- [27] Semenov A D, Nebosis R S, Gousev Yu P, Heusinger M A and Renk K F 1995 *Phys. Rev. B* **52** 581
- [28] Ekström H and Karasik B S 1995 *Appl. Phys. Lett.* **66** 3212
- [29] Balanis C A 1985 *Antenna Theory, Analysis and Design* (New York: Wiley)
- [30] Hansen R C 1992 *Proc. IEEE* **80** 141
- [31] Tarasov M A, Prokopenko G V, Ovsyannikov G A, Serpuchenko I L, Filippenko L V, Koshelets V P, Polyansky O Yu and Vystavkin A N 1994 *Proc. SPIE* **2250** 291
- [32] Elantev A I and Karasik B S 1989 *Sov. J. Low Temp.*

- Phys.* **16** 145  
Ekström H, Karasik B S, Kollberg E and Yngvesson K S  
1995 *IEEE Trans. Microwave Theory Technol.* **43** 936
- [33] Sergeev A V, Semenov A D, Kouminov P, Trifonov V A,  
Goghidze I G, Karasik B S, Goltsman G N and  
Gershenzon E M 1994 *Phys. Rev. B* **49** 9091
- [34] Lindgren M, Trifonov V, Zorin M, Danerud M, Winkler D,  
Karasik B S, Gol'tsman G N and Gershenzon E M 1994  
*Appl. Phys. Lett.* **64** 3036
- [35] Karasik B S, McGrath W R, Gaidis M C, Burns M J,  
Kleinsasser A W, Delin K A and Vasquez R P 1996  
*Proc. 7th Int. Symp. on Space Terahertz Technology*  
(Charlottesville, VA) (Charlottesville, VA: University of  
Virginia Press)